Computer Systems
Science and Engineering

Tech Science Press

DOI: 10.32604/csse.2023.036744
Article

A Unique Discrete Wavelet & Deterministic Walk-Based Glaucoma Classification Approach Using Image-Specific Enhanced Retinal Images

Krishna Santosh Naidana and Soubhagya Sankar Barpanda*

School of Computer Science and Engineering, VIT-AP University, Inavolu, Beside AP Secretariat, Amaravati-522237, AP, India

*Corresponding Author: Soubhagya Sankar Barpanda. Email: soubhagya.barpanda@vitap.ac.in
Received: 11 October 2022; Accepted: 21 December 2022; Published: 26 May 2023

Abstract: Glaucoma is a group of ocular atrophy diseases that cause progressive vision loss by affecting the optic nerve. Because of its asymptomatic nature, glaucoma has become the leading cause of human blindness worldwide. In this paper, a novel computer-aided diagnosis (CAD) approach for glaucomatous retinal image classification has been introduced. It extracts graph-based texture features from structurally improved fundus images using discrete wavelet-transformation (DWT) and deterministic tree-walk (DTW) procedures. Retinal images are considered from both public repositories and eye hospitals. Images are enhanced with image-specific luminance and gradient transitions for both contrast and texture improvement. The enhanced images are mapped into undirected graphs using DTW trajectories formed by the image's wavelet coefficients. Graph-based features are extracted from these graphs to capture image texture patterns. Machine learning (ML) classifiers use these features to label retinal images. This approach has attained an accuracy range of 93.5% to 100%, 82.1% to 99.3%, 95.4% to 100%, 83.3% to 96.6%, 77.7% to 88.8%, and 91.4% to 100% on the ACRIMA, ORIGA, RIM-ONE, Drishti, HRF, and HOSPITAL datasets, respectively. The major strength of this approach is texture pattern identification using various topological graphs. It has achieved optimal performance with SVM and RF classifiers using biorthogonal DWT combinations on both public and patients' fundus datasets. The classification performance of the DWT-DTW approach is on par with the contemporary state-of-the-art methods, which can be helpful for ophthalmologists in glaucoma screening.

Keywords: Wavelet-transformation; glaucoma classification; deterministic tree walk; graph-based features

1 Introduction

Glaucoma is an incurable retinal distortion caused by an increase in intraocular pressure (IOP) due to uneven generation and flowing "aqueous humor" [1]. A thorough examination of the retinal

structures such as the optic disc (OD) and the cup (OC) can prevent glaucoma. Expert ophthalmologists clinically examine the human eye for glaucoma using several practices, such as fundus (retinal) image structural analysis [2]. However, these are tedious and error-prone due to their non-mechanical nature. As technology advances, CAD has become a standard medical practice for ophthalmologists in making quick and accurate glaucoma diagnoses. The CAD follows a fixed approach that contains major phases such as retinal image pre-processing, region-of-interest (ROI) segmentation, feature extraction, and classification using artificial intelligence (AI) approaches. The initial CAD phase is pre-processing, which usually eliminates noise existing in the image and applies various approaches to enhance the retinal image for a clear structural view. The feature extraction phases identify significant texture patterns in enhanced images for auto-screening by AI approaches.

In contrast to ordinary images, the structural analysis of fundus images is highly sophisticated due to the complex retinal tissue textures. In most cases, the textures of both the glaucomatous and healthy eyes are usually similar, and their discrimination requires a high level of cognitive processing. In the proposed CAD approach, complex texture analysis has been carried out on qualitatively improved retinal images using the combination of DTW and DWT for proper identification of the glaucomatous eye. It extracts the significant retinal texture patterns for the accurate designation of glaucomatous images. The rest of the paper is presented in different sections: Section 2 gives existing CAD-based glaucoma detection approaches that are motivated for the proposed approach; Section 3 demonstrates the proposed retinal image enhancement and the new feature extraction approach for glaucoma image classification; Section 4 investigates the classification results for scientific findings, and; Section 5 concludes the paper with the future work.

2 Existing Glaucoma Practices and Motivation

There are currently several existing works in the field of CAD-based glaucoma classification. This section presents a detailed investigation of them in terms of CAD's major phases: image pre-processing, feature extraction, and classification. Muthmainah et al. [3] extracted first-order statistical (FoS) features from contrast-limited adaptive histogram equalization (CLAHE)-based enhanced retinal images. Then these features are ranked and fed to support vector machines (SVM) and k-nearest neighbor (k-NN) approaches for glaucoma screening. Afterward, Belgacem et al. [4] extracted the cup/disc ratio (CDR) of retinal images for glaucoma identification. Later, principal component analysis (PCA) features are extracted by Christopher et al. [5] to diagnose the glaucoma progression. Next, both texture and structural features are extracted by An et al. [6] using Visual Geometry Group (VGG)-19-based transfer learning (TL) approaches, and the classification is done with a random forest (RF) classifier. Subsequently, Rehman et al. [7] extracted statistical and fractal features from denoised and edge-enhanced images for glaucoma identification using SVM, RF, Ada, and RusBoost ML approaches. Later, an anisotropic diffusion filter is utilized by Mohamed et al. [8] for retinal image denoising before correcting image illumination. Then, the enhanced images' super-pixel-based features were classified using the SVM classifier. Afterward, Oh et al. [9] collected retinal features using a convolutional neural network (CNN) along with the visual field (VF) test characteristics and then selected using a chi-square test. SVM, RF, and XGBoost classifiers were used in their study. Thomas et al. [10] then applied artificial neural networks (ANN) to human eye visual fields for glaucoma screening. Later, Thakur et al. [11] extracted both structural features such as CDR from vessel-free retinal images and non-structural features of different orders from grayscale images. These features are ranked and classified using Naive Bayes (NB), SVM, k-NN, and RF classifiers. Next, histogram-based (HE) enhanced retinal images are segmented by Shanmugam et al. [12] using an adaptive network (Au-Net) for OD and OC proportions. Nawaldgi et al. [13] extracted the co-occurrence matrix of gray-level (GLCM) characteristics. Then, DWT features were extracted from

electro-retinography signals by Gajendran et al. [14]. ML classifiers used these DWT features for early-stage glaucoma detection. Patel et al. [15] then split the color channels of retinal images into bit-planes to generate local-binary patterns (LBP) for classification. Later, the retinal image color channels' LBP features were extracted and classified using SVM by Rebinth et al. [16]. Next, Arsyan et al. [17] extracted invariant moment features from the HE-enhanced retinal OC and blood vessels. Then k-NN is applied by considering the five nearest neighbors. Table 1 summarizes the literature survey done for the proposed method.

Table 1: Summarization of the state-of-the-art approaches

Reference & year	Performance measures	Observations
[3], 2018	Acc: 93.3%, Spe: 93.3%, Sen: 93.3%	CLAHE may over-enhance some portions of the retinal image.
[4], 2018	Acc: 96%	The number of features is limited.
[5], 2018	AUC: 95%	The other variants, two-dimensional (2D)-PCA and $2D^2$-PCA did not test.
[6], 2019	AUC: 96.3%	A single classifier was used without image pre-processing.
[7], 2019	Acc: 99.3%, Spe: 99.4%, Sen: 96.9%	Image pre-processing is done without regard for the time or frequency domains.
[8], 2019	Acc: 98.6%, Spe: 92.3%, Sen: 97.6%	The super-pixel approach may lead to unintentional image artifacts.
[9], 2019	Acc: 94.7%, Spe: 95.0%, Sen: 94.1%	Image pre-processing has not been applied.
[10], 2019	Sen & Spe: > 95%	This experiment did not include retinal pictures.
[11], 2020	Acc: 97.2%, Spe: 96%, Sen: 97%	Except for SVM, the remaining classifiers did not perform well with the extracted features.
[12], 2021	Acc: 99%, Spe: 95%, Sen: 86%	Due to limitations (over-enhancement) of HE enhancement, the OD and OC region identification may not be optimal.
[13], 2022	Acc: 88.86%	Image enhancement approaches did not employ.
[14], 2022	Acc: 91.6%, Spe: 91.6%, Sen: 91.6%	The wavelet specifications have not been given.
[15], 2022	Acc: 95.04%, Spe: 96.3%, Sen: 93.7%	There was no image pre-processing.
[16], 2022	Acc: 80.77%, Spe: 77.38%, Sen: 80.5%	Image enhancement may improve the performance of this approach.
[17], 2022	Acc: 81.4%	The HE approach over-enhances image textures.

Note: Acc: Accuracy, Spe: Specificity, Sen: Sensitivity, AUC: Area under the receiver operating characteristic curve.

2.1 The Proposed Approach's Contributions

The in-depth literature survey has identified some CAD phase-wise research limitations such as ***Image pre-processing***: (i) Most of the pre-processing approaches were designed for gray-scale medical images, (ii) The parameter values for enhancement were manually assigned, (iii) Texture intensity and structure improvement did not address jointly; ***Feature extraction & classification***: (i) Image features have extracted without or with minimal usage of time- or frequency-domains, (ii) Most of the feature extraction approaches are limited by constraints such as threshold values, image dimensions, and directions, (iii) Inter-pixel relations are extracted with simple mathematical operations, and (iv) Texture patterns are extracted by considering only immediately adjacent pixels.

The proposed CAD approach has been motivated and designed to address the identified limitations with the following contributions:

Image pre-processing:

- Color retinal images' brightness and texture improvement are jointly considered.
- Image-specific parameters are scientifically calculated and employed in the enhancement.

Feature extraction and classification:

- Retinal image textures are analyzed using orthogonal (e.g., Daubechies (Db)) and biorthogonal (e.g., Bior Nr. Nd or Bi Nr. Nd) wavelets.
- Texture patterns have been extracted using graph theory and traveler's walks for various memory constraints.
- Texture pattern extraction considers both immediate and non-immediate neighboring pixels.
- All significant graph-based features are extracted to build powerful feature vectors.

3 The Proposed CAD Glaucoma Approach

In this study, retinal images were considered from various public datasets: ACRIMA [18] (396: glaucomatous, 309: normal), ORIGA [19] (168: glaucomatous, 482: normal), RIM-ONE [19] (325: glaucomatous, 458: normal), Drishti [16] (70: glaucomatous, 31: normal), and HRF [16] (15: glaucomatous, 15: normal). Furthermore, patients' retinal images (110: glaucomatous, 110: normal) are collected from the Goutami Eye Institute [20] (HOSPITAL) to test the proposed approach's performance. This approach has balanced retinal image illumination and structure improvement, and extracted pixel intensity relationships using DTW on graphs generated from DWT of images. DWT is a time-frequency localization approach. It explores the frequency and spatial information concurrently from the given 2D input image using a decimation operation with wavelet filter banks. High-pass and low-pass filters in filter banks extract details and approximate information from fundus images in the form of wavelet coefficients. The DTW operation can be interpreted as a tourist planning to visit randomly located locations on a multi-dimensional graph (map). The traveler begins his journey at a given point and proceeds to the next-nearest place in a deterministic manner, i.e., move to the next-nearest place that has not been visited in the most recent steps. This travel can explore neighboring relationship patterns that characterize the given map. The overall procedure is shown in Fig. 1 and explained in the following sub-sections.

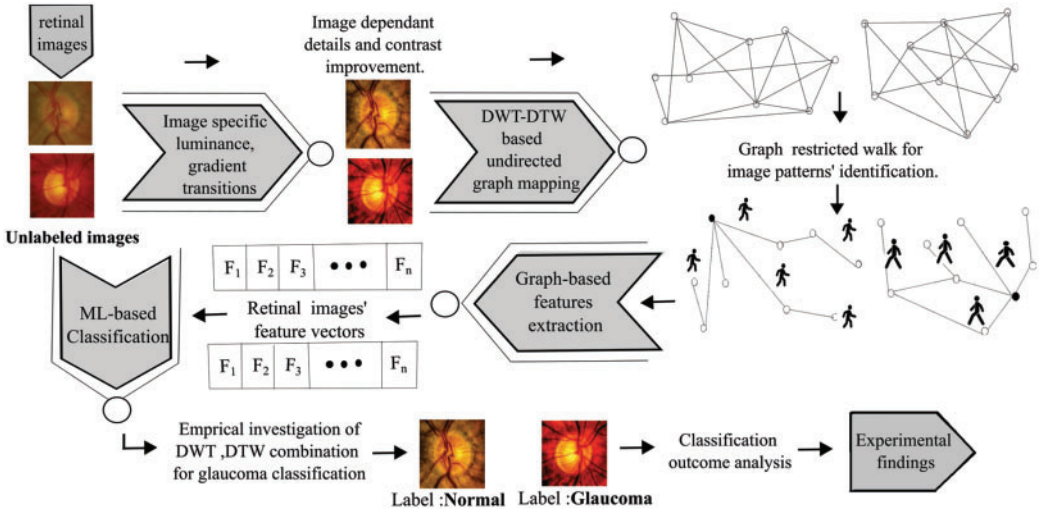

Figure 1: The procedural flow of the DWT-DTW-based glaucoma classification approach

3.1 Retinal Image Pre-Processing

The proposed pre-processing has been divided into two stages: Image visual quality improvement and details enhancement. The entire approach is given in *Algorithm 1* (***A₁***) and explained w.r.t step numbers (***A₁: Sₙ***). In this study, image edges are preserved by the *Regional Laplacian-Filtering* (RLF) approach that constructs Gaussian-pyramid (GP) for each image (I_{RGB}) resolution. It extracts image lower-resolutions level by level (GP_{level}) (***A₁: S₁***) by successive down-sampling. The discriminating details of each successive GP_{level} are used to generate Laplacian-pyramid levels (LP_{level}). The RLF is applied image-level-wise as well as coefficient-wise. These are designated by the position (p_r, p_c) and pyramid levels (p_l) (***A₁: S₂***), using three stages:

- ***Stage 1: Remapping computation***: Each sub-region (SR_l) is processed with a remapping computation $C(.)$ using C_{sd} and $C_{se,}$ operations and τ. The value τ represents p_l-level GP coefficient at the position (p_r, p_c). The C_{sd} modifies finer scale details by using $s_f(v)$, which is generated by intensity variation (σ_{iv}), noise level (nl), mean (Mu), and standard deviation (Sd) of the image. Using the image average entropy (Ent_{avg}), the C_{se}changes edge amplitudes. Then image sub-region remapping ($C(SR_l)$) is defined using a simple point-wise operation.
- ***Stage 2: SR-pyramid generation***: Generates a Laplacian pyramid $LP[C(SR_l)]$ for $C(SR_l)$.
- ***Stage 3: Updating the output pyramid*:** The generated level-wise LP coefficients, i.e., $LP_l[C(SR_l)]$ (p_r, p_c) are assigned to the output (TI), i.e., $LP_l[TI](p_r, p_c)$.

It is followed by a series of image-specific luminance and gradient modulations on TI_{RGB}(***A₁: S₃***). The **luminance transaction (LT)** is carried out by mapped luminance levels (G_{R_Yd}) using a luminance-level ordered set, $G_{Yd} = \{ld_1, ld_2, \ldots, ld_{n-1}\}$. The G_{Yd} is defined as the pair-wise differences of $Y_{sort}I_{RGB} = \{l_1, l_2, \ldots, l_n\}$ and a mapped luminance-level set $G_{R_{Yd}} = \{rd_1, rd_2, \ldots rd_{n-1}\}$. Image luminance enhancement is followed by structural (OD, OC, and blood vessels) improvement using **gradient transition (GT)** on LT outcome i.e., LME_{IMG}. In GT, image gradients $SI_{\partial f_x}$ and $SI_{\partial f_y}$ are employed using a new gradient inflation function (I_{fun}) that operates on pixel values (p_v) at each (p_r, p_c) location. Finally, $SI_{\partial f_x}$ and $SI_{\partial f_y}$ are integrated (by collapsing) to form complete enhanced retinal images (RI_{FE}) (***A₁: S₄***).

Algorithm 1: Pre-processing of retinal image

Input: Color retinal image (I_{RGB}).

Process:

- **Step 1: Resolution**$_{Low-Degree}$ $(\boldsymbol{I_{RGB}}) \leftarrow [\boldsymbol{GP}\,(\boldsymbol{I_{RGB}})]$
- **Step 2: for all** (p_r, p_c, p_l) **do**

$$\textbf{Stage 1: } \boldsymbol{SR_l} \leftarrow \boldsymbol{C_{\tau,\sigma_{iv}}}\,(\boldsymbol{SR_l})$$

$$\begin{array}{l} where, \quad \mathbf{C}\,(\mathbf{j}) = \mathbf{C_{sd}}\,(\mathbf{j}), \quad if\ \langle |j-\tau| \le \sigma_{iv} \rangle \quad else \quad \mathbf{C_{se}}\,(\mathbf{j}), \\ \Rightarrow \mathbf{C_{sd}}\,(\mathbf{j}) = \tau + signum\,(j-\tau)\,\sigma_{iv} s_f\,(|j-\tau|/\sigma_{iv}), \ \text{where} \\ \mathrm{s}_f(v) = ((q1 * sm1 + q2 * sm2)/2) * v^{\gamma} + (1 - (q1 * sm1 + q2 * sm2)/2) * v \\ sm1 = (v * \sigma_{iv} - nl)/(2 * nl - nl); \quad sm2 = (v - Mu)/Sd, 0 < nl < 1, \\ \Rightarrow \mathbf{C_{se}}\,(\mathbf{j}) = \tau + sgf\,(j-\tau)\left(e_f\,(|j-\tau| - \sigma_{iv}) + \sigma_{iv}\right), \quad e_f(v) = Ent_{avg} * v \end{array}$$

$$\textbf{Stage 2:}\boldsymbol{LP} \leftarrow \boldsymbol{LP}\,[\boldsymbol{C}\,(\boldsymbol{SR_l})]$$

$$\textbf{Stage 3:}\boldsymbol{LP_l}\,[\boldsymbol{TI}]\,(\boldsymbol{p_r}, \boldsymbol{p_c}) \leftarrow \boldsymbol{LP_l}\,[\boldsymbol{C}\,(\boldsymbol{SR_l})]\,(\boldsymbol{p_r}, \boldsymbol{p_c})$$

end

- **Step 3:** $\boldsymbol{LME_{IMG}}\,(\boldsymbol{lm_t}) = \boldsymbol{F_{\text{Trans}}}\,(\boldsymbol{l_t}) = \boldsymbol{l_t} + \left(\dfrac{\textbf{Entropy}(\boldsymbol{I_{RGB}})}{\max(\boldsymbol{G_{Yd}}) - \min(\mathbf{G_{Yd}})}\right) * \sum_{v=1}^{t-1} (\boldsymbol{rd_v} - \boldsymbol{ld_v})$

$$\begin{array}{c} 1 \le t \le n, \qquad G_{R\_Yd} = \{rd_1, rd_2, \ldots rd_{n-1}\}, \ where \\ rd_g = ai + \left(rd_g - ai\right)^{\max(G_{Yd}) - \min(G_{Yd})}, \ \ ai = mean(\mathrm{G}_{Yd}) * \min(\mathrm{G}_{Yd}) \end{array}$$

$$\boldsymbol{SI}_{\partial f_x, \partial f_y}(\boldsymbol{p_r}, \boldsymbol{p_c}) = \partial \boldsymbol{f}_{x,y}(\boldsymbol{p_r}, \boldsymbol{p_c}).\, \boldsymbol{I_{fun}}\,(\boldsymbol{p_v})$$

$$\begin{array}{c} I_{fun}\,(p_v) = \sum_{w=1}^{w\max} (-1)^w \dfrac{(C_r)^{w - w\max}}{\mathrm{w}.\,(median\,(LME_{IMG}))!}\,(p_v)^w, 3 \le w_{\max} \le 5, \\ C_r = \sum_{c=R,G,B} \min\,(LME_{IMG}\,(c)) + [\max\,(LME_{IMG}\,(c)) - \min\,(LME_{IMG}\,(c))] \end{array}$$

- **Step 4:** $\boldsymbol{RI_{FE}} \leftarrow \textbf{Integration}_{\text{collapsing}}(\boldsymbol{SI_{\partial f_x}}, \boldsymbol{SI_{\partial f_y}})$

Output: An illumination-corrected & structurally improved retinal image: RI_{FE}.

3.2 The Proposed Retinal Image Feature Extraction

The objective is to extract retinal image (i.e., RI_{FE}) texture patterns using various Db and Bior Nr. Nd wavelets and tourists' walks. As per the existing literature, our proposed approach is the first one that extracts DWT and DTW-based retinal image features for glaucoma classification. In this approach, an undirected graph constructed with DTW trajectories formed using the image's DWT coefficients of $W_r \times W_c$ size. According to graph theory, a retinal image-mapped graph (I_G) is formed by a vertex-set (V_s) and an edge-set (E_s), i.e., $IG = (V_s, E_s)$. The mapping is carried out in two phases: V_s generation and E_s construction. Initially, each RI_{FE}'s DWT coefficient is mapped to a vector V_s. In the next stage, a tourist walks among the vertices (V_s) using the partially self-avoiding property that forms trajectory paths based on various reminisces (i.e., memory) (R_M) values. Since the objective of feature extraction is to retrieve significant image texture relationship patterns, it uses distance and similarity measures to identify neighboring vertices as shown in Fig. 2. The distance is measured using a weighted Euclidean distance (E_{D_c}) approach. Weights were generated using cosine similarity between coefficients. For each source vertex (S_v), the neighborhood (Nh) co-vertex count has been determined using the radius (R), i.e., $N_c = \sum_{r=1}^{R} 8 * r$ as shown in Fig. 2e.

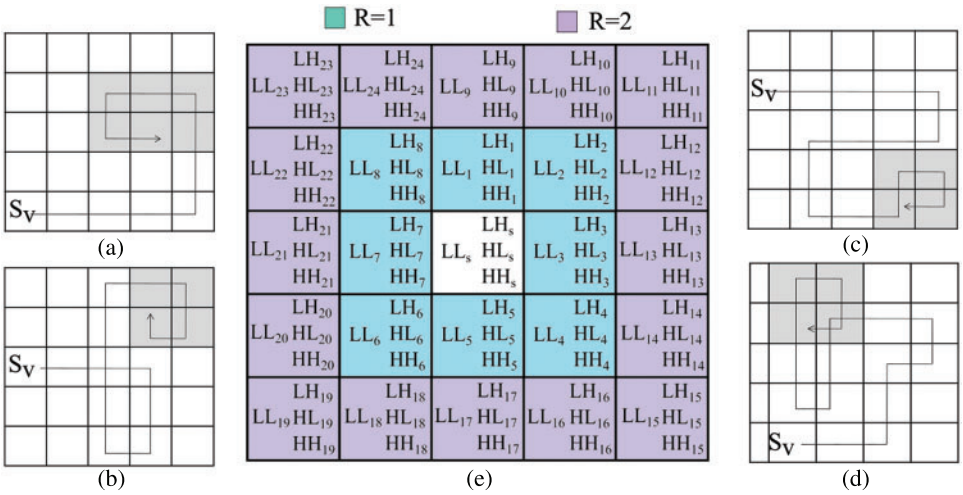

Figure 2: The neighborhood test for various '*R*' values along with sample DTW whirlpool trajectories

As shown in Eq. (1), the distance covered by R between the source (center) and participating (P_s) vertices is calculated by a metric E_{Dp} using vertex positions.

$$E_{Dp} = \left(W_s\left(\left(x_s - x_p\right)^2 + \left(y_s - y_p\right)^2\right)\right)^{\frac{1}{2}},\ p = 1\ to\ N_c \tag{1}$$

where (x_s, y_s) is the S_v vertex position, and (x_p, y_p) is the P_s vertex position. The weight function, W_s is measured using cosine similarity between positional DWT coefficients using Eq. (2),

$$W_s = SB_s * SB_p / \sqrt{\sum SB_s^2} * \sqrt{\sum SB_p^2},\quad SB \in \{LL, LH, HL, HH\} \tag{2}$$

where LL_s, LH_s, HL_s, and HH_s are DWT coefficients of S_v and LL_p, LH_p, HL_p, and HH_p are DWT coefficients of P_s. The E_{Dp} values are generated for each pair of S_v and P_s. In this approach, the first eight closest neighbors (N_{Vs}) are considered for each V_s from the neighborhood participation set N_{ps} based on E_{Dp} values.

$$N_{Vs} = \left\{V_{p1}, \ldots, V_{p8}\right\},\ E_{Dp_1} < \ldots < E_{Dp_8} < E_{D_{other}},\ E_{D_{other}} \notin N_{Vs}\ ,\ E_{D_{other}} \in N_{Ps} \tag{3}$$

Tourists' walks start by considering each vertex $v \in V_s$ to generate corresponding DTW trajectories. These were controlled by a dual-rule moving protocol (MP) as given in Eq. (4). The first rule is that each movement should consider the nearest neighbor according to the distance measured using Eq. (1). The other is that, while considering a vertex as the nearest neighbor for the movement, it should not have been visited in the previous R_M number of steps.

$$MP = V_{pn}, if \left\langle \begin{matrix} Rule1 : \left(V_{pn} \in N_{Vs}\ \&\ \mathrm{E}_{Dp}\left(\mathrm{V}_{Pn}\right) < \mathrm{E}_{Dp}\left(\mathrm{V}_{Pi}\right), \mathrm{i} = 1, \ldots, 8\ \&\ \mathrm{n} \neq \mathrm{i}\right) \\ Rule2 : V_{pn}\ not\ visited\ in\ last\ R_M\ steps \end{matrix} \right\rangle \tag{4}$$

where, V_{pn} is the next vertex in visiting list. The DTW will continue to visit vertices one-by-one by the MP until they reach the whirlpool situation. It occurs when a tourist continually visits the same vertex series without escaping.

Detection of a whirlpool in DTW is a challenging task. During the DTW progression, a vertex can revisit. According to the second rule of MP, in the current step, recently visited vertices (from

the last R_M steps) cannot be considered. Sample whirlpool situations have shown in Figs. 2a–2d, and their early detection can save computing resources. A new policy has been adopted for the detection of whirlpool situations. It is based on the sequence of vertices revisited during DTW, as shown in Fig. 3. Our policy has utilized a 1D vector M_{wp} to keep track of visited vertices and a structure S_{wp} for each vertex that records the number of times it has been visited. The whirlpool identification policy (I_{policy}) is designed using Eq. (5).

$$I_{policy} = \text{WP},\ if\ \left[\left(V_{pr} > P_{\max}, V_{pr} \in M_{wp}\right) \vee \left(V_{sc} >= L_{\max}, V_{sc} \in S_{wp}\right) \vee \left(||T|| == A_{\max}\right)\right] \tag{5}$$

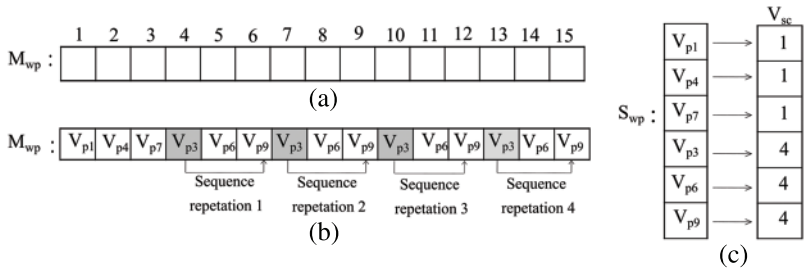

Figure 3: (a) The track of DTW's visited vertices (b) an example of a situation that can lead to a whirlpool for the DTW trajectory (c) vertex's visited record structure

This policy covers three situations: (1) the maximum number of times (P_{max}), a vertex pattern (V_{pr}) appears; (2) a vertex visited step count (V_{sc}) with a maximum limit (L_{max}), and; (3) the DTW trajectory T that covers the maximum area A_{max}.

In the proposed approach, P_{max} and L_{max} values are 3 and 5 respectively. The maximum edge count (A_{max}) is set at 25, to avoid boundless paths. Once a whirlpool occurs, DTW progression stops, and the vertices covered in that journey form a trajectory corresponding to that V_s. This process repeats for all available vertices in V_s. Finally, an undirected graph (RI_G) is constructed by considering all these DTW trajectories corresponding to each vertex. The proposed approach has generated individual RI_G for different R_M values. Retinal image texture patterns are then captured using graph-based features (Table 2) of RI_G.

Table 2: Graph-based features and their significance in texture pattern identification

S. no	Features	Description
1	Average degree (D_{avg})	Similar categories of retinal images can have nearly identical vertex degrees and texture patterns: $D_{avg}^{Rm} = \sum_{i=1}^{\|\|V_s\|\|} \deg(v_i) / \|\|V_s\|\|, v_i \in V_s$
2	Joint degree entropy (E_{jd}):	This is the entropy of similar degree (JD_M) DWT coefficient connections: $E_{jd}^{R_M} = -\sum_{i=1}^{size(JD_M,1)} \sum_{j=1}^{size(JD_M,2)} P(JD_M(i,j)) * \log_2 P(JD_M(i,j))$

(Continued)

Table 2: Continued

S. no	Features	Description
3	Link density (L_d):	It measures the ratio of DWT-coefficient connections to the total number of possible connections: $L_d^{R_M} = 2 * \|\|E_s\|\| / (\|\|V_s\|\| * \|\|V_s\|\| - 1)$
4	Average closeness centrality (CC_{avg}):	It measures the DWT coefficients' ability to spread the pattern information using the shortest path (SP): $CC_{avg}^{R_M} = \|\|V_s\|\| / \sum_{i,j=1}^{\|\|V_s\|\|} sp\left(v_i, v_j\right),\ i \neq j\ and\ v_i, v_j \in V_s$
5	Graph entropy (E_g):	It finds the information quantity spread among DWT coefficients: $E_g^{R_M}(RI_G) = \min_{v_x, v_y}\left(Entropy(v_x)/Entropy(v_x \mid v_y)\right),\ v_x \in V_s$, v_y: A set with v_x
6	Average clustering coefficient (A_{cc}):	It finds the degree of the DWT coefficient to form a cluster using $Nh\ (Z_{v_i}) : A_{CC}^{R_M} = mean\left(2\left\|\left\{e_{lm} : v_l, v_m \in Z_{v_i}, e_{lm} \in E_s\right\}\right\| / \left\|\left\|Z_{v_i}\right\|\right\| * \left(\left\|\left\|Z_{v_i}\right\|\right\| - 1\right)\right),\ v_i \in V_s$
7	Eigen centrality (C_e):	The significance of each DWT coefficient in the graph is measured: $C_e^{R_M} = 1/\lambda \sum_{y \in RI_G} A_{x,y} v_y$, λ: constant, $A_{x,y}$: Adjacent matrix.
8	Page rank average (P_{avg}):	It measures the importance of a DWT coefficient: $P_{avg}^{R_M} = mean\left((1/2\left\|E_s\right\|)\left[\deg(v_1), \ldots, \deg(v_n)\right]\right),\ v_i \in V_s$
9	Meshedness coefficient (M_c):	The cyclic relationships among DWT coefficients are determined: $M_C^{R_M} = (\|\|E_s\|\| - \|\|V_s\|\|) + 1/(2 * \|\|V_s\|\|) - 5$
10	Average hop count (H_{avg}):	It measures the average SP lengths between pairs of DWT coefficients: $H_{avg}^{R_M} = (1/\|\|V_s\|\| * (\|\|V_s\|\| - 1)) * \sum_{i \neq j} sp\left(v_i, v_j\right)$
11	Eccentricity (E_c):	It identifies the longest texture patterns: $E_c^{R_M} = \max\left(DISTANCE\left(v_s, v_o\right)\right), v_s, v_o \in V_s,$ and $s \neq o$

Using these graph-based features corresponding to each RI_G, a feature vector is constructed for each retinal image. This study considers R_M values from 1 to 6.

$$FV_{RI_G} = \left\{D_{avg}^{R_M}, E_{jd}^{R_M}, L_d^{R_M}, CC_{avg}^{R_M}, E_g^{R_M}, C_{v_i}^{R_M}, C_e^{R_M}, P_{avg}^{R_M}, M_C^{R_M}, H_{avg}^{R_M}, E_c^{R_M}\right\}, 1 \leq R_M \leq 6 \quad (6)$$

All extracted FV_{RI_G} are supplied to ML classifiers for glaucoma screening. The following section presents the obtained results and the corresponding analysis.

4 Results and Analysis

The entire experiment was carried out on the ROI (i.e., OC and OD areas) of color retinal images. The whole procedural flow is shown in Fig. 4. Initially, the retinal images' intensity is improved using the image-specific edge and details modifier controllers C_{se} and C_{sd} of the RLF approach. Then LT and GT operations are applied for luminance enhancement and texture improvement, respectively. Image-specific parameter-based preprocessing produces better-quality retinal images than existing methods, such as LM&GM [21] and CLAHE [22]. Some sample results are shown in Fig. 5. When

compared to the CLAHE and LM&GM approaches, the qualitative results show strong evidence for both luminance and structural image improvement.

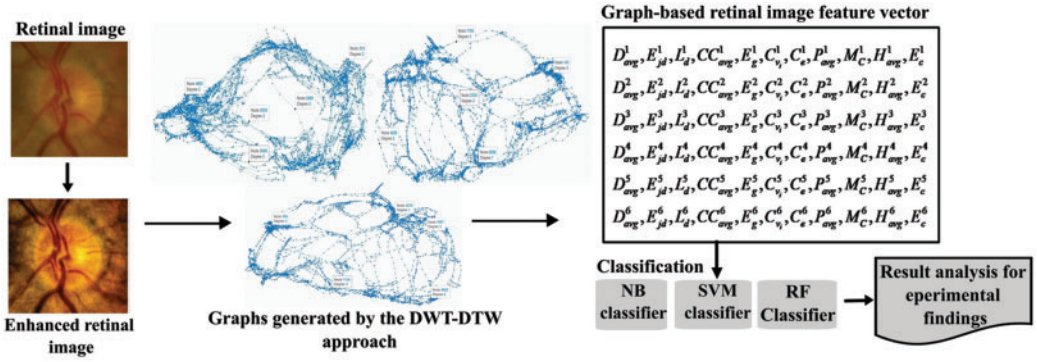

Figure 4: The block diagram of the proposed glaucoma screening approach

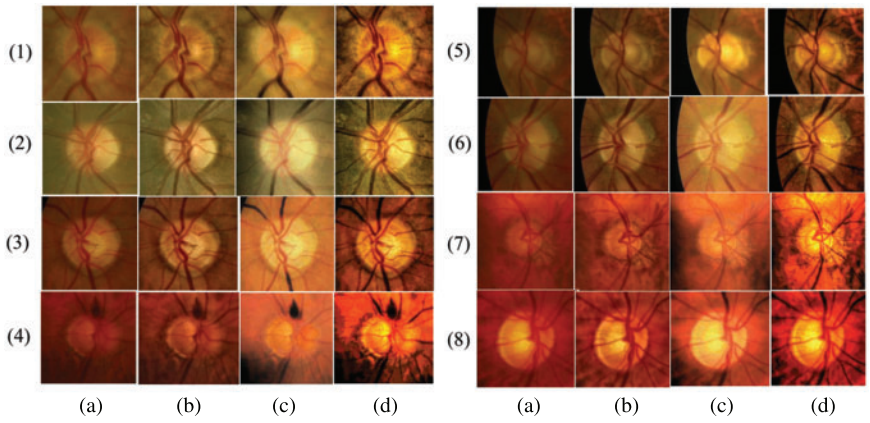

Figure 5: (a) Original input images, (b), (c), and (d) enhanced images by CLAHE, LM&GM, and the proposed pre-processing

The quantitative assessment of the proposed enhancement approach is carried out using three quality metrics: (i) **Structural Similarity Index (SS_Index):** It measures the image similarity, which is a product of image structure, contrast, and luminance, (ii) **Mean Square Error (MSE):** It measures the difference between original and enhanced images. A lower MSE value indicates qualitative image enhancement, and (iii) **Blind Image Spatial quality (BIS):** It is a blind (no reference) image spatial measurement for image quality. It returns a non-negative value between [0, 100]. The lower value indicates a better qualitative image. All these measures for the same sample images from Fig. 5 are reported in Table 3.

The histogram plots in Fig. 6 show the performance of the proposed enhancement over other existing approaches. The proposed enhancement keeps the images' texture similarity (Fig. 6a) much closer to the original images, and the MSE values (Fig. 6b) are significantly lower than those of the CLAHE and LM&GM-based enhanced images. The proposed methodology has achieved qualitatively enhanced retinal images in terms of spatial measurement, i.e., BIS (Fig. 6c), compared to the other approaches.

Table 3: Quantitative assessment of the proposed enhancement approach

S. no.	Quality metric	CLAHE	LM& GM	The proposed method	S. no.	Quality metric	CLAHE	LM& GM	The proposed method
1	**SS_Index**	0.8140	0.9273	**0.9709**	5	**SS_Index**	0.6712	0.8998	**0.9304**
	MSE	0.0549	0.0295	**0.0053**		**MSE**	0.1887	0.0942	**0.0097**
	BIS	28.2382	32.9776	**24.7823**		**BIS**	35.7184	36.1886	**36.1711**
2	**SS_Index**	0.6094	0.7965	**0.9238**	6	**SS_Index**	0.6266	0.8700	**0.9722**
	MSE	0.1608	0.0799	**0.0095**		**MSE**	0.1357	0.0674	**0.0074**
	BIS	40.7023	35.1752	**31.5075**		**BIS**	39.8451	32.2539	**29.0974**
3	**SS_Index**	0.6417	0.8689	**0.9608**	7	**SS_Index**	0.7100	0.9583	**0.9647**
	MSE	0.1801	0.0883	**0.0051**		**MSE**	0.0607	0.0304	**0.0054**
	BIS	34.7092	36.1509	**30.4678**		**BIS**	49.5250	46.9446	**42.3555**
4	**SS_Index**	0.8615	0.9636	**0.9880**	8	**SS_Index**	0.7282	0.8582	**0.9448**
	MSE	0.0385	0.0202	**0.0079**		**MSE**	0.0603	0.0311	**0.0053**
	BIS	40.1846	31.6877	**24.4849**		**BIS**	39.3425	34.2647	**25.4082**

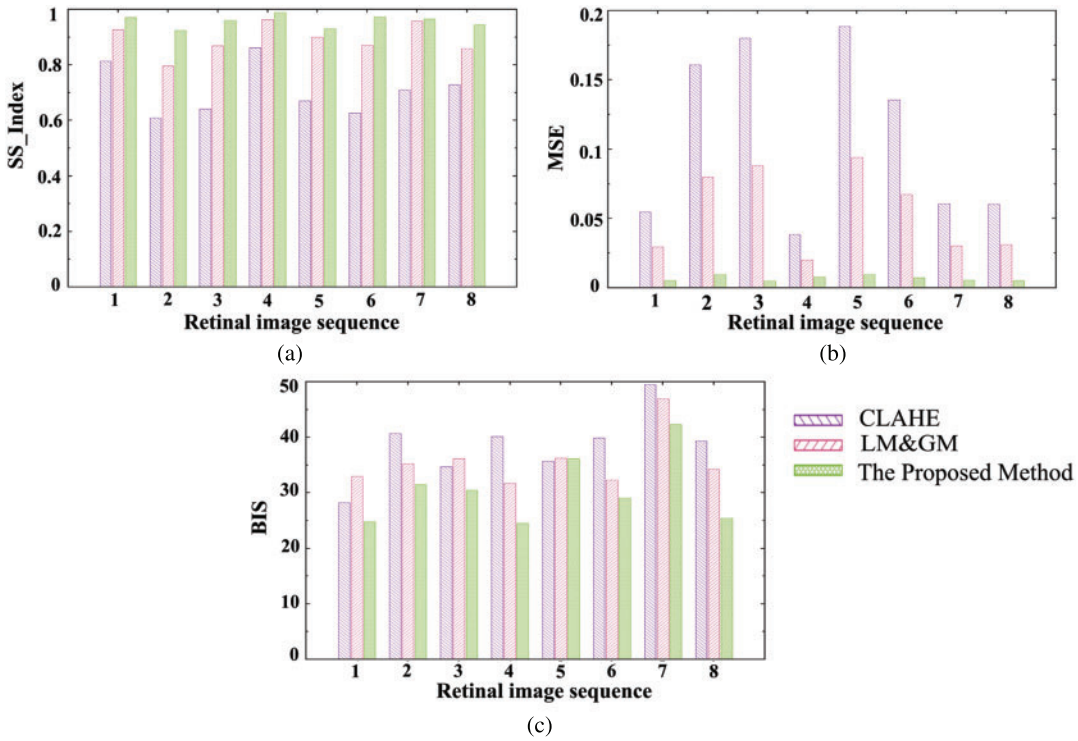

Figure 6: Image quality assessment plots by various measures: (a) SS_Index, (b) MSE, and (c) BIS

In this approach, six undirected graphs are built for each retinal image, accounting for all R_M values using DTW trajectories. Sample retinal image-mapped graphs (for images in Fig. 5) are shown

in Fig. 7. Each DWT and R_M combination produced a distinct topological complex graph. This crucial property enables the proposed approach to retrieve significant texture patterns. The architecture of each graph depends on the images' DWT coefficient inter-relationships. Unlike conventional graphs, the DWT-DTW-based graph's structurality will dynamically change according to the image's texture, which can capture all possible patterns. This characteristic of the DWT-DTW approach is essential for analyzing retinal (medical) image textures.

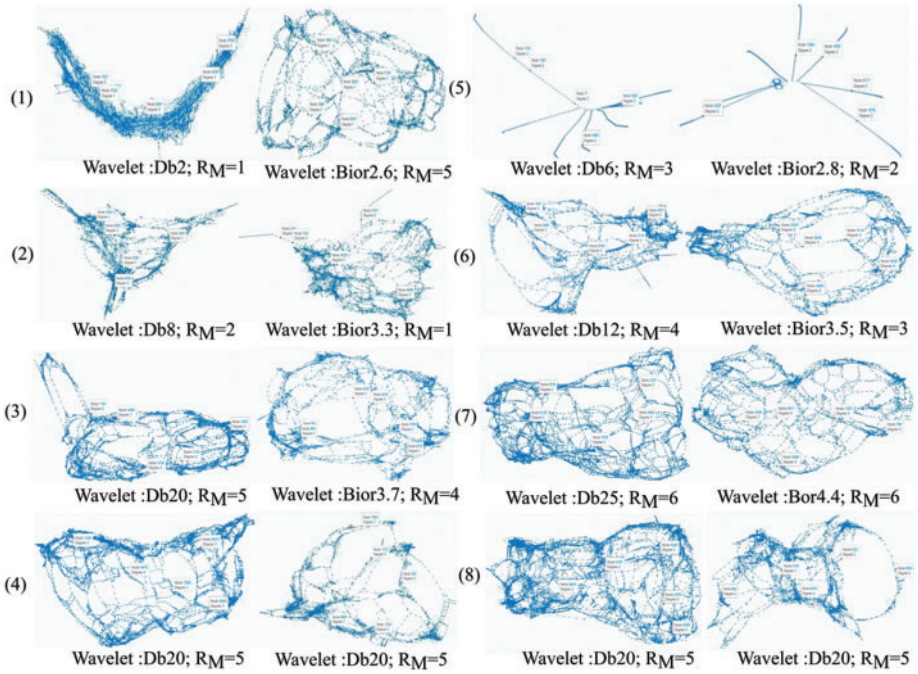

Figure 7: Sample graphs generated from retinal image mapping using the DWT-DTW approach

Once all the DWT-DTW graphs are generated, graph-based features are extracted to form feature vectors (FV_{RI_G}). The obtained feature vectors have been randomly split using a 70:30 proportion without replacement for training and testing by NB, SVM, and RF classifiers. Various wavelets (DWT and DTW) are used in this study to achieve optimal glaucoma screening. The glaucoma classification results from various datasets are presented in Table 4 in terms of percentages. In the case of ACRIMA, both SVM and RF classifiers have achieved 100% accuracy, while the NB classifier's performance is moderately low for various wavelets. Despite the high true-positive prediction rates of SVM and RF classifiers, all these are vulnerable to false-negative predictions. The DWT-DTW approach has achieved a higher accuracy range, i.e., above 96%, with biorthogonal wavelets than with orthogonal wavelets. In this approach, the NB classifier achieved 98.1% accuracy with the ORIGA dataset, while the SVM and RF classifiers secured 99.3% accuracy. The SVM and RF classifiers have high true-negative prediction rates with ORIGA data, but all classifiers suffer from false-positive predictions. Especially with orthogonal wavelets, the DWT-DTW approach has a lower true-positive rate than biorthogonal wavelets. This approach has achieved the highest accuracy on RIM-ONE data since the dataset size was considerably larger than the remaining datasets. In this case, SVM classifiers suffer from minor false-negative predictions, while RF classifiers have a maximum true-negative prediction rate. Through the DWT-DTW approach, all three classifiers suffer from minor false-positive predictions. However, orthogonal and biorthogonal wavelets are well suited to this

approach with RIM-ONE data. Based on patient retinal images collected from the hospital, the proposed DWT-DTW method performs admirably. The highest accuracies achieved by NB, SVM, and RF classifiers are 97.1%, 98.5%, and 100%, respectively. This proposed approach has lower false-positive prediction rates than false-negative predictions with the hospital data. With the NB classifier, this approach has achieved mixed responses with both wavelet types. However, the combination of biorthogonal wavelet DWT-DTW with the SVM and RF classifiers performs better than orthogonal wavelets on the patient data. In the case of the Drishti dataset, the maximum accuracy attained by all three classifiers is 96.6%. This approach's performance is relatively high even with smaller datasets like HRF. Overall, the proposed DWT-DTW method has attained maximum performances with the SVM and RF classifiers for all instances. The corresponding performance graphs are shown in Fig. 8.

Table 4: Glaucoma classification results using the DWT-DTW approach

	ACRIMA									ORIGA								
	NB			SVM			RF			NB			SVM			RF		
	Acc	Sen	Spe	Acc	Sen	Spe	Acc	Sen	Spe	Acc	Sen	Spe	Acc	Sen	Spe	Acc	Sen	Spe
Db2	93.5	100	84.7	96.4	100	91.5	97.8	100	94.9	91.2	82.1	93.1	93.8	76.0	100	96.2	78.5	100
Db4	94.2	100	86.4	98.5	100	96.6	99.2	100	98.3	91.2	85.7	92.4	97.5	85.7	100	96.8	82.1	100
Db6	95.7	100	89.8	98.5	100	96.6	99.2	100	98.3	93.1	85.7	94.6	96.8	82.1	100	96.8	82.1	100
Db8	98.5	100	96.6	100	100	100	100	100	100	97.5	92.8	98.4	97.5	85.7	100	96.8	82.1	100
Db10	98.5	100	96.6	99.2	100	98.3	99.2	100	98.3	98.1	96.4	98.4	98.1	89.2	100	98.1	89.2	100
Db12	96.4	100	91.5	97.1	100	93.2	100	100	100	98.1	96.4	98.4	98.1	89.2	100	98.1	89.2	100
Db15	96.4	100	91.5	97.8	100	94.9	99.2	100	98.3	97.5	96.4	97.7	98.1	89.2	100	98.1	89.2	100
Db20	96.4	100	91.5	98.5	100	96.6	100	100	100	97.5	96.4	97.7	98.1	89.2	100	98.1	89.2	100
Db30	97.8	98.7	96.6	99.2	100	98.3	100	100	100	97.5	96.4	97.7	97.5	85.7	100	97.5	85.7	100
Db32	97.8	98.7	96.6	100	100	100	100	100	100	97.5	96.4	97.7	97.5	85.7	100	97.5	85.7	100
Db40	98.5	100	96.6	100	100	100	100	100	100	95	89.2	96.2	98.1	89.2	100	97.5	85.7	100
Db42	98.5	100	96.6	100	100	100	99	100	97.8	95.6	92.8	96.2	98.1	89.2	100	97.5	85.7	100
Bi2.6	96.4	100	91.5	97.1	100	93.2	98.5	100	96.6	96.2	92.8	96.9	97.5	85.7	100	98.1	89.2	100
Bi2.8	97.1	100	93.2	99.2	100	98.3	100	100	100	96.8	92.8	97.7	98.1	89.2	100	98.7	92.8	100
Bi3.3	98.5	100	96.6	100	100	100	100	100	100	96.8	96.4	96.9	99.3	96.4	100	99.3	96.4	100
Bi3.5	98.5	100	96.6	100	100	100	100	100	100	96.8	96.4	96.9	99.3	96.4	100	99.3	96.4	100
Bi3.7	98.5	100	96.6	99.2	100	98.3	100	100	100	97.5	96.4	97.7	99.3	96.4	100	99.3	96.4	100
Bi4.4	97.1	100	93.2	100	100	100	99.2	100	98.3	93.1	85.7	94.6	99.3	96.4	100	96.2	78.5	100
Bi5.5	98.5	100	96.6	99.2	100	98.3	100	100	100	93.1	85.7	94.6	97.5	85.7	100	99.3	96.4	100
Bi6.8	98.5	100	96.6	99.5	100	98.9	100	100	100	96.2	92.8	96.9	98.1	89.2	100	99.3	96.4	100

	RIM-ONE									HOSPITAL								
	NB			SVM			RF			NB			SVM			RF		
	Acc	Sen	Spe	Acc	Sen	Spe	Acc	Sen	Spe	Acc	Sen	Spe	Acc	Sen	Spe	Acc	Sen	Spe
Db2	95.2	98.9	92.7	99.1	97.9	100	99.1	97.9	100	92.8	97.1	88.5	92.8	97.1	88.5	92.8	97.1	88.5
Db4	98.7	97.9	99.2	99.1	97.9	100	99.5	98.9	100	95.7	97.1	94.2	97.1	97.1	97.1	97.1	97.1	97.1
Db6	98.2	97.9	98.5	99.5	98.9	100	100	100	100	95.7	100	91.4	98.5	97.1	100	98.5	97.1	100
Db8	98.7	97.9	99.2	100	100	100	100	100	100	95.7	100	91.4	98.5	97.1	100	98.5	97.1	100
Db10	98.7	97.9	99.2	100	100	100	100	100	100	97.1	100	94.2	98.5	97.1	100	98.5	97.1	100
Db12	97.8	97.9	97.8	100	100	100	100	100	100	94.2	97.1	91.4	95.7	97.1	94.2	95.7	97.1	94.2
Db15	97.4	97.9	97	99.5	98.9	100	99.5	98.9	100	94.2	97.1	91.4	95.7	97.1	94.2	95.7	97.1	94.2

(Continued)

Table 4: Continued

	RIM-ONE									HOSPITAL								
	NB			SVM			RF			NB			SVM			RF		
	Acc	Sen	Spe	Acc	Sen	Spe	Acc	Sen	Spe	Acc	Sen	Spe	Acc	Sen	Spe	Acc	Sen	Spe
Db20	97	97.9	96.3	99.1	97.9	100	99.5	98.9	100	95.7	100	91.4	97.1	97.1	97.1	97.1	97.1	97.1
Db30	95.7	97.9	94.1	97.8	97.9	97.8	100	100	100	97.1	97.1	97.1	94.2	97.1	91.4	94.2	97.1	91.4
Db32	97	97.9	96.3	99.1	97.9	100	99.1	97.9	100	91.4	97.1	85.7	97.1	97.1	97.1	97.1	97.1	97.1
Db40	97	97.9	96.3	100	100	100	100	100	100	94.2	97.1	91.4	95.7	97.1	94.2	94.2	94.2	94.2
Db42	97	97.9	96.3	99.5	98.9	100	100	100	100	91.4	97.1	85.7	94.2	94.2	94.2	94.2	94.2	94.2
Bi2.6	98.2	97.9	98.5	99.1	97.9	100	99.5	98.9	100	91.4	97.1	85.7	97.1	97.1	97.1	97.1	97.1	97.1
Bi2.8	98.2	97.9	98.5	99.1	97.9	100	100	100	100	92.8	100	85.7	97.1	97.1	97.1	97.1	97.1	97.1
Bi3.3	98.7	97.9	99.2	100	100	100	100	100	100	94.2	100	88.5	94.2	97.1	91.4	97.1	97.1	97.1
Bi3.5	97.8	98.9	97	99.5	98.9	100	99.5	98.9	100	92.8	100	85.7	95.7	97.1	94.2	98.5	97.1	100
Bi3.7	98.7	97.9	99.2	99.5	98.9	100	100	100	100	92.8	100	85.7	94.2	97.1	91.4	97.1	97.1	97.1
Bi4.4	97.4	97.9	97	100	100	100	100	100	100	95.7	100	91.4	97.1	97.1	97.1	100	100	100
Bi5.5	97.8	98.9	97	100	100	100	100	100	100	95.7	100	91.4	98.5	97.1	100	98.5	97.1	100
Bi6.8	98.2	97.9	98.5	99.5	98.9	100	100	100	100	97.1	100	94.2	98.5	97.1	100	98.5	97.1	100
	DRISHTI									HRF								
	NB			SVM			RF			NB			SVM			RF		
	Acc	Sen	Spe	Acc	Sen	Spe	Acc	Sen	Spe	Acc	Sen	Spe	Acc	Sen	Spe	Acc	Sen	Spe
Db2	86.6	85	90	76.6	65	100	73.3	60	100	55.5	50	60	66.6	75	60	66.6	75	60
Db4	90	90	90	90	85	100	76.6	65	100	66.6	75	60	66.6	75	60	77.8	50	100
Db6	93.3	90	100	90	85	100	96.6	95	100	77.7	75	80	88.9	75	100	88.8	75	100
Db8	96.6	95	100	86.6	80	100	96.6	95	100	88.9	75	100	88.9	75	100	88.8	75	100
Db10	96.6	95	100	90	85	100	93.3	90	100	88.9	75	100	88.9	75	100	88.8	100	80
Db12	93.3	90	100	96.6	95	100	93.3	90	100	77.7	75	80	77.7	75	80	77.8	50	100
Db15	90	90	90	83.3	75	100	93.3	90	100	66.6	75	60	77.7	75	80	77.8	50	100
Db20	83.3	90	70	93.3	90	100	93.3	90	100	66.6	75	60	77.7	75	80	77.8	50	100
Db30	80	80	80	90	85	100	90	90	90	66.6	75	60	77.7	75	80	66.6	75	60
Db32	90	85	100	90	85	100	90	90	90	66.6	75	60	77.7	75	80	66.6	75	60
Db40	80	85	70	90	85	100	90	90	90	66.6	75	60	77.7	75	80	66.6	75	60
Db42	83.3	85	80	90	85	100	90	90	90	66.6	75	60	77.7	75	80	77.8	50	100
Bi2.6	83.3	80	90	93.3	90	100	93.3	90	100	77.7	75	80	88.8	1000	80	77.8	100	60
Bi2.8	90	85	100	93.3	90	100	93.3	90	100	77.7	75	80	77.7	75	80	77.8	100	60
Bi3.3	96.6	95	100	96.6	95	100	96.6	95	100	88.8	100	80	88.8	1000	80	88.8	75	100
Bi3.5	93.3	90	100	90	85	100	93.3	90	100	88.8	100	80	77.7	75	80	77.8	50	100
Bi3.7	93.3	95	90	96.6	95	100	96.6	95	100	88.8	100	80	77.7	75	80	77.8	50	100
Bi4.4	96.6	95	100	96.6	95	100	93.3	90	100	77.7	75	80	77.7	75	80	88.8	100	80
Bi5.5	96.6	95	100	93.3	90	100	96.6	95	100	77.7	75	80	88.8	1000	80	88.8	100	80
Bi6.8	96.6	95	100	96.6	95	100	96.6	95	100	77.7	75	80	88.8	1000	80	88.8	100	80

Notes: Acc: Accuracy, Spe: Specificity, Sen: Sensitivity.

Due to the moderate patient data size, the NB classifier has attained lower classification accuracy than other cases. In this DWT-DTW approach, the performance plots of all classifiers with RIM-ONE data are more consistent and reliable. More fluctuations are seen in classification accuracy plots by orthogonal wavelets than by biorthogonal wavelets. Referring to the other classification measures, the proposed approach has more stable true-negative prediction rates (i.e., specificity) than true-positive prediction rates (i.e., sensitivity). Because regularity improves with the order, all performance plots

hit the minimal values only with the lower-order orthogonal wavelets rather than with the higher-order orthogonal and biorthogonal wavelets. The corresponding confusion matrix metrics, such as true and false positives and negatives, are shown in Table 5. The proposed approach has either 0 or 1 false-negative prediction, with a maximum of 9 false-positive predictions for the ACRIMA dataset. In the case of ORIGA data, the approach has both types of false predictions with the NB classifier but zero false-positive predictions with other classifiers. This approach has very few incorrect predictions with RIM-ONE data. The proposed approach has generated a considerably lower range of incorrect predictions in the patient retinal dataset case. In the case of the Drishti dataset, the approach has higher true-negative predictions by all three classifiers. This approach also achieved steady, correct predictions with the HRF dataset.

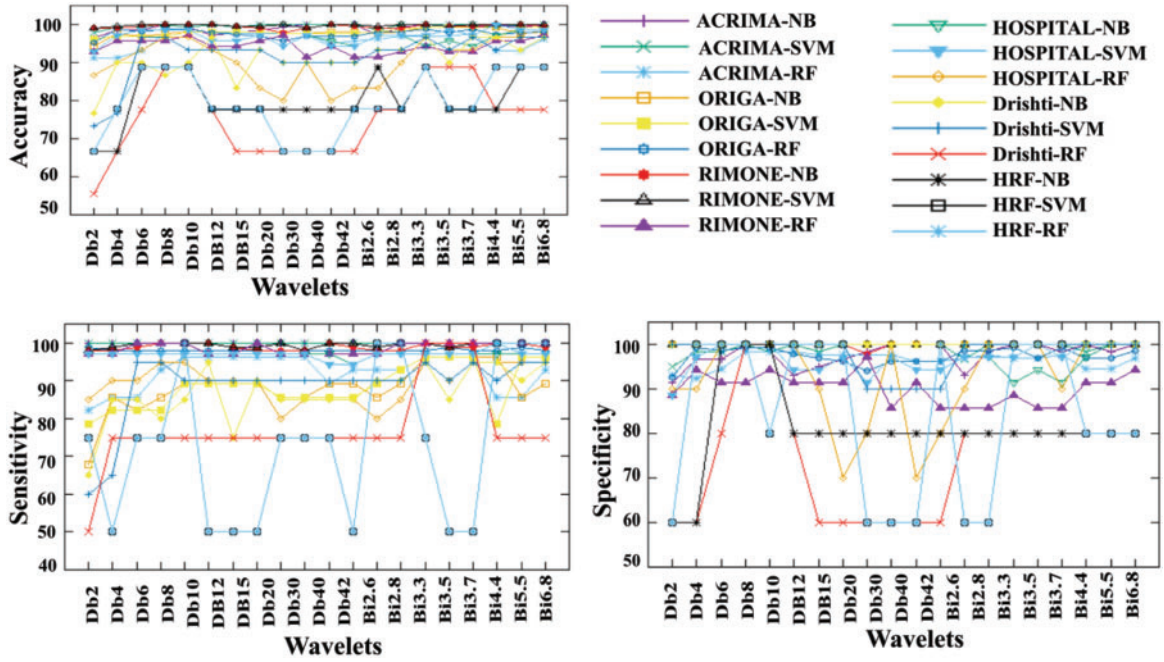

Figure 8: The DWT-DTW glaucoma classification (a) accuracy, (b) sensitivity, and (c) specificity graphs

Table 5: Confusion matrix metrics by DWT-DTW-based glaucoma classification

	ACRIMA												ORIGA											
	NB				SVM				RF				NB				SVM				RF			
	Tp	Fp	Fn	Tn	Tp	Fp	Fn	Tn	Tp	Fp	Fn	Tn	Tp	Fp	Fn	Tn	Tp	Fp	Fn	Tn	Tp	Fp	Fn	Tn
Db2	118	13	0	79	118	7	0	85	117	5	1	87	39	6	11	139	38	0	12	145	43	0	7	145
Db4	118	12	0	80	118	3	0	89	118	2	0	90	39	6	11	139	45	0	5	145	44	0	6	145
Db6	118	9	0	83	118	3	0	89	118	2	0	90	40	3	10	142	44	0	6	145	44	0	6	145
Db8	118	3	0	89	118	0	0	92	118	0	0	92	46	1	4	144	45	0	5	145	44	0	6	145
Db10	118	3	0	89	118	2	0	90	118	2	0	90	48	1	2	144	47	0	3	145	49	0	1	145
Db12	118	7	0	85	118	6	0	86	118	0	0	92	48	1	2	144	47	0	3	145	49	0	1	145
Db15	118	7	0	85	117	5	1	87	118	2	0	90	46	1	4	144	47	0	3	145	49	0	1	145
Db20	118	7	0	85	118	4	0	88	118	0	0	92	46	1	4	144	45	0	5	145	49	0	1	145

(Continued)

Table 5: Continued

	ACRIMA												ORIGA											
	NB				SVM				RF				NB				SVM				RF			
	Tp	Fp	Fn	Tn	Tp	Fp	Fn	Tn	Tp	Fp	Fn	Tn	Tp	Fp	Fn	Tn	Tp	Fp	Fn	Tn	Tp	Fp	Fn	Tn
Db30	117	5	1	87	118	2	0	90	118	0	0	92	46	1	4	144	45	0	5	145	45	0	5	145
Db32	117	5	1	87	118	0	0	92	118	0	0	92	46	1	4	144	45	0	5	145	45	0	5	145
Db40	118	4	0	88	118	0	0	92	118	0	0	92	43	2	7	143	44	0	6	145	45	0	5	145
Db42	118	4	0	88	118	0	0	92	118	2	0	90	43	1	7	144	44	0	6	145	45	0	5	145
Bi2.6	118	7	0	85	118	6	0	86	118	4	0	88	44	1	6	144	45	0	5	145	49	0	1	145
Bi2.8	118	6	0	86	118	2	0	90	118	0	0	92	45	1	5	144	44	0	6	145	48	0	2	145
Bi3.3	118	4	0	88	118	0	0	92	118	0	0	92	45	1	5	144	49	0	1	145	49	0	1	145
Bi3.5	118	4	0	88	118	0	0	92	118	0	0	92	45	1	5	144	49	0	1	145	49	0	1	145
Bi3.7	118	4	0	88	118	2	0	90	118	0	0	92	45	1	5	144	49	0	1	145	49	0	1	145
Bi4.4	118	6	0	86	118	0	0	92	118	2	0	90	40	3	10	142	49	0	1	145	43	0	7	145
Bi5.5	118	4	0	88	118	2	0	90	118	0	0	92	40	3	10	142	45	0	5	145	49	0	1	145
Bi6.8	118	4	0	88	118	1	0	91	118	0	0	92	44	1	6	144	49	0	1	145	4	0	1	145

	RIM-ONE												HOSPITAL											
	NB				SVM				RF				NB				SVM				RF			
	Tp	Fp	Fn	Tn	Tp	Fp	Fn	Tn	Tp	Fp	Fn	Tn	Tp	Fp	Fn	Tn	Tp	Fp	Fn	Tn	Tp	Fp	Fn	Tn
Db2	96	10	1	127	95	0	2	137	95	0	2	137	34	4	1	31	34	4	1	31	34	4	1	31
Db4	95	1	2	136	95	0	2	137	96	0	1	137	34	2	1	33	34	1	1	34	34	1	1	34
Db6	95	2	2	135	96	0	1	137	97	0	0	137	35	3	0	32	34	0	1	35	34	0	1	35
Db8	95	1	2	136	97	0	0	137	97	0	0	137	35	3	0	32	34	0	1	35	34	0	1	35
Db10	95	1	2	136	97	0	0	137	97	0	0	137	35	2	0	33	34	0	1	35	34	0	1	35
Db12	95	3	2	134	97	0	0	137	97	0	0	137	34	3	1	32	34	2	1	33	34	2	1	33
Db15	95	4	2	133	96	0	1	137	96	0	1	137	34	3	1	32	34	2	1	33	34	2	1	33
Db20	95	5	2	132	95	0	2	137	96	0	1	137	35	3	0	32	34	1	1	34	34	1	1	34
Db30	95	8	2	129	95	3	2	134	97	0	0	137	34	1	1	34	34	3	1	32	34	3	1	32
Db32	95	5	2	132	95	0	2	137	95	0	2	137	34	5	1	30	34	1	1	34	34	1	1	34
Db40	95	5	2	132	97	0	0	137	97	0	0	137	34	3	1	32	34	2	1	33	33	2	2	33
Db42	95	5	2	132	96	0	1	137	97	0	0	137	34	5	1	30	33	2	2	33	33	2	2	33
Bi2.6	95	2	2	135	95	0	2	137	96	0	1	137	34	5	1	30	34	1	1	34	34	1	1	34
Bi2.8	95	2	2	135	95	0	2	137	97	0	0	137	35	5	0	30	34	1	1	34	34	1	1	34
Bi3.3	95	1	2	136	97	0	0	137	97	0	0	137	35	4	0	31	34	3	1	32	34	1	1	34
Bi3.5	96	4	1	133	96	0	1	137	96	0	1	137	35	5	0	30	34	2	1	33	34	0	1	35
Bi3.7	95	1	2	136	96	0	1	137	97	0	0	137	35	5	0	30	34	3	1	32	34	1	1	34
Bi4.4	95	4	2	133	97	0	0	137	97	0	0	137	35	3	0	32	34	1	1	34	35	0	0	35
Bi5.5	96	4	1	133	97	0	0	137	97	0	0	137	35	3	0	32	34	0	1	35	34	0	1	35
Bi6.8	95	2	2	135	96	0	1	137	97	0	0	137	35	2	0	33	34	0	1	35	34	0	1	35

	DRISHTI												HRF											
	NB				SVM				RF				NB				SVM				RF			
	Tp	Fp	Fn	Tn	Tp	Fp	Fn	Tn	Tp	Fp	Fn	Tn	Tp	Fp	Fn	Tn	Tp	Fp	Fn	Tn	Tp	Fp	Fn	Tn
Db2	17	1	3	9	13	0	7	10	12	0	8	10	2	2	2	3	3	2	1	3	3	2	1	3
Db4	18	1	2	9	17	0	3	10	13	0	7	10	3	2	1	3	3	2	1	3	2	0	2	5
Db6	18	0	2	10	17	0	3	10	19	0	1	10	3	1	1	3	3	0	1	5	3	0	1	5
Db8	19	0	1	10	16	0	4	10	19	0	1	10	3	0	1	5	3	0	1	5	3	0	1	5
Db10	19	0	1	10	17	0	3	10	18	0	2	10	3	0	1	5	3	0	1	5	4	1	0	4
Db12	18	0	2	10	19	0	1	10	18	0	2	10	3	1	1	3	3	1	1	3	2	0	2	5
Db15	18	1	2	9	15	0	5	10	18	0	2	10	3	2	1	3	3	1	1	3	2	0	2	5
Db20	18	3	2	7	18	0	2	10	18	0	2	10	3	2	1	3	3	1	1	3	2	0	2	5

(Continued)

Table 5: Continued

	DRISHTI												HRF											
	NB				SVM				RF				NB				SVM				RF			
	Tp	Fp	Fn	Tn	Tp	Fp	Fn	Tn	Tp	Fp	Fn	Tn	Tp	Fp	Fn	Tn	Tp	Fp	Fn	Tn	Tp	Fp	Fn	Tn
Db30	16	2	4	8	17	0	3	10	18	1	2	9	3	2	1	3	3	1	1	3	3	2	1	3
Db32	17	0	3	10	17	0	3	10	18	1	2	9	3	2	1	3	3	1	1	3	3	2	1	3
Db40	17	3	3	7	17	0	3	10	18	1	2	9	3	2	1	3	3	1	1	3	3	2	1	3
Db42	17	2	3	8	17	0	3	10	18	1	2	9	3	2	1	3	3	1	1	3	2	0	2	5
Bi2.6	16	1	4	9	18	0	2	10	18	0	2	10	3	1	1	3	3	1	1	3	4	2	0	3
Bi2.8	17	0	3	10	18	0	2	10	18	0	2	10	3	1	1	3	3	1	1	3	4	2	0	3
Bi3.3	19	0	1	10	19	0	1	10	19	0	1	10	4	1	0	4	3	0	1	5	3	0	1	5
Bi3.5	18	0	2	10	17	0	3	10	18	0	2	10	4	1	0	4	3	1	1	3	2	0	2	5
Bi3.7	19	1	1	9	19	0	1	10	19	0	1	10	4	1	0	4	3	1	1	3	2	0	2	5
Bi4.4	19	0	1	10	19	0	1	10	18	0	2	10	3	1	1	3	3	1	1	3	4	1	0	4
Bi5.5	19	0	1	10	18	0	2	10	19	0	1	10	3	1	1	3	3	1	1	3	4	1	0	4
Bi6.8	19	0	1	10	19	0	1	10	19	0	1	10	3	1	1	3	3	1	1	3	4	1	0	4

Notes: Tp: True positives, Fp: False positives, Tn: True negatives, Fn: False negatives.

The proposed DWT-DTW glaucoma classification approach's performance has been compared with similar state-of-the-art methods, as shown in Table 6. Irrespective of feature extraction approaches, the SVM classifier is widely used. Several approaches have attained an accuracy range above 97% with the RIM-ONE dataset. The highest classification measures reported [23] among existing methods are 97.6% accuracy, 94.33% sensitivity, and 99.09% specificity in various cases. The application of the time-frequency domain (i.e., DWT) is utilized by several approaches [24] and [25] for feature extraction. In the case of patient retinal data, the performance of the existing approaches [26] and [27] is moderately low.

Table 6: Performance appraisal of the glaucoma screening state-of-the-art approaches

Ref. & year	Approach	Performance				
		Dataset	Classifier	Acc (%)	Sen (%)	Spe (%)
[11] 2020	Structural and non-structural-based hybrid features.	RIM-ONE, DRISHTI	SVM	97.2	97	96
			RF	94.4	94	93
			NB	89.6	88	89
[23] 2021	Fourier-Bessel series-based EWT approach	RIM-ONE	RF	97.6	94.33	99.09
			SVM	90	90	90
[24] 2020	Empirical WT (EWT)-based GLCM features.	RIM-ONE	SVM	93.65	93.5	96.67
[25] 2020	Flexible analytic DWT-based approach	ORIGA	SVM	92.92	94.04	92.53
		RIM-ONE		90.76	94.5	87.84
[26] 2020	DWT-based statistical and texture features.	Hospital images	k-NN	89.4	87.9	90.9
		HRF		96.9	93.3	100

(Continued)

Table 6: Continued

Ref. & year	Approach	Performance				
		Dataset	Classifier	Acc (%)	Sen (%)	Spe (%)
[27] 2021	Gradient boosting-based structural features.	Hospital images	DT	89	74.5	95.6
[28] 2021	DWT-based histogram features.	HRF and MESSIDOR	SVM	93.14	79.4	94.7
[29] 2021	2D-DWT-based GLCM features.	RIM-ONE	k-NN	92.5	93.10	95.20
[30] 2021	Gradient histogram and DWT-based features.	HRF	ELM	96.5	86.9	93.8
[31] 2022	DWT-based statistical features.	RIM-ONE	SVM	91.22	85.51	98.50
[32] 2022	Multimodal Fusion-based approach.	ACRIMA	SVM	90.12	90	91
			RF	89.27	89	89
			NB	83.26	83	83
		ORIGA	SVM	77.14	75	76
			RF	79.52	76	78
			NB	68.57	65	69
The DWT-DTW glaucoma classification (The proposed method).		**ACRIMA**	**NB**	**98.5**	**100**	**96.6**
			SVM	**100**	**100**	**100**
			RF	**100**	**100**	**100**
		ORIGA	**NB**	**98.1**	**96.4**	**98.4**
			SVM	**99.3**	**96.4**	**100**
			RF	**99.3**	**96.4**	**100**
		RIM-ONE	**NB**	**98.7**	**97.9**	**99.2**
			SVM	**100**	**100**	**100**
			RF	**100**	**100**	**100**
		HOSPITAL	**NB**	**97.1**	**100**	**94.2**
			SVM	**98.5**	**97.1**	**100**
			RF	**100**	**100**	**100**
		Drishti	**NB**	**96.6**	**95**	**100**
			SVM	**96.6**	**95**	**100**
			RF	**96.6**	**95**	**100**
		HRF	**NB**	**88.8**	**100**	**80**
			SVM	**88.8**	**80**	**100**
			RF	**88.8**	**75**	**100**

Notes: Acc: Accuracy, Spe: Specificity, Sen: Sensitivity.

In the proposed approach, using DWT-DTW-based retinal image features, NB classifiers attained 98.5%, 98.1%, 98.7%, 96.6%, 88.8%, and 97.1% accuracies on the ACRIMA, ORIGA, RIM-ONE, Drishti, HRF, and HOSPITAL datasets, respectively. The SVM and RF classifiers attained similar

performance, i.e., 100%, 99.3%, 100%, 96.6%, 88.8%, and 98%–100% accuracy on the considered datasets, respectively. In the case of patients' retinal datasets, this approach has attained 97% accuracy with extremely high correct prediction rates.

The optimal performance of the DWT-DTW method is due to an extensive retinal texture enhancement and analysis, which offers the following benefits:

- Pre-processing:
    1. **Balanced enhancement**: Images' textures, as well as illumination, are jointly improved.
    2. **Image-dependent enhancement**: The enhancement process considered image-specific details rather than manually supplied constant values.
- Feature extraction and classification:
    1. **In-depth time-frequency analysis**: An extensive image's time-frequency domain analysis has been done using various wavelets for texture identification.
    2. **Image's specific pattern exploration**: Image texture-dependent methodologies (such as image-mapped graphs) are utilized in pattern extraction.
    3. **Diversified texture analysis**: Each image texture is analyzed in various dimensions using special techniques (such as different graph architectures).
    4. **Robust performance**: The classification performs well on public retinal repositories and patients' retinal data.

These advantages are compared with the state-of-the-art approaches (from Table 6). The summarized report has been given in Table 7. It shows a strong reason for using the DWT-DTW method for glaucoma classification rather than existing approaches.

Further, the phase-wise research findings of the proposed CAD-based glaucoma screening method are as follows:

- **Retinal image pre-processing:** (i) Qualitative retinal images have been generated due to enhancement of the images' luminance and texture; (ii) The suggested approach improves the images without affecting the original texture using image-specific characteristics.
- **Retinal image feature extraction:** (i) DTW trajectories corresponding to various wavelets' coefficients and R_M values enable us to extract significant image texture patterns; and (ii) Various topological graphs make the texture analysis powerful.
- **Retinal image classification:** (i) Biorthogonal wavelet-based graph features are stronger for glaucoma classification than orthogonal wavelets; (ii) SVM and RF classifiers have achieved high glaucoma classification accuracy.

Table 7: The state-of-the-art approaches comparison with the proposed method's advantages

Approaches/ advantages	[11]	[23]	[24]	[25]	[26]	[27]	[28]	[29]	[30]	[31]	[32]	The DWT-DTW method
Balanced enhancement	X	X	X	X	X	•	•	X	X	X	•	✓

(Continued)

Table 7: Continued

Approaches/ advantages	[11]	[23]	[24]	[25]	[26]	[27]	[28]	[29]	[30]	[31]	[32]	The DWT-DTW method
Image dependant enhancement	✓	X	X	X	X	•	•	X	✓	✓	•	✓
In-depth time-frequency analysis	X	X	X	✓	X	X	X	X	X	X	X	✓
Image's specific pattern exploration	X	✓	X	X	X	X	✓	X	✓	✓	✓	✓
Diversified texture analysis	✓	✓	X	X	X	X	✓	X	✓	✓	✓	✓
Robust performance	X	X	X	X	X	X	X	X	X	X	X	✓

Notes: ✓: Achieved, **X**: Not Achieved, **•:** The corresponding CAD phase is not included.

Overall, it has been determined that the combination of the biorthogonal wavelet family and DTW-based graph theory is optimal for glaucoma screening.

5 Conclusions and Future Work

The proposed CAD-based glaucoma classification is a unique approach that utilizes the combination of time-frequency localization and graph theory. Images' textures are improved in a balanced way using image-dependent details. Various topological graphs have been generated for each retinal image to explore pixels' neighborhood relationships using in-depth time-frequency analysis. It identifies significant directional texture patterns for accurate screening. Results have proven that the proposed enhancement improves the images' quality without altering their texture patterns. The proposed DWT-DTW-based glaucoma screening has achieved an average accuracy of 99.5%, 98.9%, 99.56%, 96.6%, 88.8%, and 98.5%, sensitivity of 100%, 96.4%, 99.3%, 95%, 100%, and 99.03%, and specificity of 98.06%, 99.4%, 99.7%, 100%, 80%, and 98.06% on the ACRIMA, ORIGA, RIM-ONE, Drishti, HRF, and HOSPITAL datasets, respectively. Our approach has achieved optimal performance for biorthogonal DTW and RF or SVM classifiers combination. Moreover, the DWT-DTW method has achieved highly satisfactory classification accuracy in the case of patient data. The performance of the proposed method has been compared with state-of-the-art methods, and its performance is far better than existing methodologies. Thus, this CAD approach will become a powerful aid for ophthalmologists in providing faster and more accurate glaucoma screening. However, the proposed approach has fewer limitations, which include that the classification accuracy is slightly lower with smaller datasets and that this approach suffers from incorrect predictions for some combinations. These limitations will be addressed in our future work using multi-level graph CNNs.

Acknowledgement: The fundus images used in this study were given by the Goutami Eye Institute, Rajamahendravaram-533105, Andhra Pradesh, India. We would like to express our deep and sincere gratitude to Dr. Y. Srinivas Reddy, M.S. (Ophthal), and Dr. A. Prasanth Kumar, M.S. (Ophthal), for providing corresponding information and the fundus images.

Funding Statement: The authors received no specific funding for this study.

Conflicts of Interest: The authors declare that they have no conflicts of interest to report regarding the present study.

References

[1] J. Katz and A. P. Costarides, "Facts *vs.* fiction: The role of cannabinoids in the treatment of glaucoma," *Current Ophthalmology Reports*, vol. 7, no. 3, pp. 177–181, 2019.

[2] A. C. de Moura Lima, L. B. Maia, R. M. P. Pereira, G. B. Junior, J. D. S. de Almeida *et al.,* "Glaucoma diagnosis over eye fundus image through deep features," in *2018 25th Int. Conf. on Systems, Signals and Image Processing (IWSSIP)*, June 2018, Maribor, Slovenia, IEEE, pp. 1–4, 2018.

[3] M. U. Muthmainah, H. A. Nugroho and B. Winduratna, "Analysis of retinal fundus images for classification of glaucoma," in *2018 1st Int. Conf. on Bioinformatics, Biotechnology, and Biomedical Engineering-Bioinformatics and Biomedical Engineering*, Yogyakarta, Indonesia, IEEE, vol. 1, pp. 1–6, 2018.

[4] R. Belgacem, I. T. Malek, H. Trabelsi and I. Jabri, "A supervised machine learning algorithm SKVMs used for both classification and screening of glaucoma disease," *New Front. Ophthalmol.*, vol. 4, no. 4, pp. 1–27, 2018.

[5] M. Christopher, A. Belghith, R. N. Weinreb, C. Bowd, M. H. Goldbaum *et al.,* "Retinal nerve fiber layer features identified by unsupervised machine learning on optical coherence tomography scans predict glaucoma progression," *Investigative Ophthalmology & Visual Science*, vol. 59, no. 7, pp. 2748–2756, 2018.

[6] G. An, K. Omodaka, K. Hashimoto, S. Tsuda, Y. Shiga *et al.,* "Glaucoma diagnosis with machine learning based on optical coherence tomography and color fundus images," *Journal of Healthcare Engineering*, vol. 2019, pp. 48–57, 2019.

[7] Z. U. Rehman, S. S. Naqvi, T. M. Khan, M. Arsalan, M. A. Khan *et al.,* "Multi-parametric optic disc segmentation using super pixel-based feature classification," *Expert Systems with Applications*, vol. 120, pp. 461–473, 2019.

[8] N. A. Mohamed, M. A. Zulkifley, W. M. D. W. Zaki and A. Hussain, "An automated glaucoma screening system using cup-to-disc ratio via simple linear iterative clustering super pixel approach," *Biomedical Signal Processing and Control*, vol. 53, no. 7, pp. 101454, 2019.

[9] S. Oh, Y. Park, K. J. Cho and S. J. Kim, "Explainable machine learning model for glaucoma diagnosis and its interpretation," *Diagnostics*, vol. 11, pp. 11, 2021.

[10] P. Thomas, T. Chan, T. Nixon, B. Muthusamy and A. White, "Feasibility of simple machine learning approaches to support detection of non-glaucomatous visual fields in future automated glaucoma clinics," *Eye*, vol. 33, no. 7, pp. 1133–1139, 2019.

[11] N. Thakur and M. Juneja, "Classification of glaucoma using hybrid features with machine learning approaches," *Biomedical Signal Processing and Control*, vol. 62, pp. 102137, 2020.

[12] P. Shanmugam, J. Raja and R. Pitchai, "An automatic recognition of glaucoma in fundus images using deep learning and random forest classifier," *Applied Soft Computing*, vol. 109, pp. 107512, 2021.

[13] S. Nawaldgi and Y. S. Lalitha, "Automated glaucoma assessment from color fundus images using structural and texture features," *Biomedical Signal Processing and Control*, vol. 77, pp. 103875, 2022.

[14] M. K. Gajendran, L. J. Rohowetz, P. Koulen and A. Mehdizadeh, "Novel machine-learning based framework using electro-retinography data for the detection of early-stage glaucoma," *Frontiers in Neuroscience*, vol. 16, 2022.

[15] R. K. Patel and M. Kashyap, "Automated screening of glaucoma stages from retinal fundus images using BPS and LBP based GLCM features," *International Journal of Imaging Systems and Technology*, vol. 33, pp. 246–261, 2022.

[16] A. Rebinth and S. M. Kumar, "Glaucoma diagnosis based on color and spatial features using kernel SVM," *Cardiometry*, no. 22, pp. 508–515, 2022.

[17] A. R. Arsyan and W. F. Al Maki, "Classification of glaucoma using invariant moment methods on k-nearest neighbor and random forest models," *Building of Informatics, Technology and Science (BITS)*, vol. 3, no. 4, pp. 466–472, 2022.

[18] P. Elangovan and M. K. Nath, "Glaucoma assessment from color fundus images using convolutional neural network," *International Journal of Imaging Systems and Technology*, vol. 31, no. 2, pp. 955–971, 2021.

[19] I. J. Mac Cormick, B. M. Williams, Y. Zheng, K. Li, B. Al-Bander *et al.,* "Accurate, fast, data efficient and interpretable glaucoma diagnosis with automated spatial analysis of the whole cup to disc profile," *PloS One*, vol. 14, no. 1, pp. e0209409, 2019.

[20] Goutami Eye Institute.1, RV Nagar, Rajamahendravaram–533105, AP, India, Website: www.goutami.org

[21] C. Zhao, Z. Wang, H. Li, X. Wu, S. Qiao *et al.,* "A new approach for medical image enhancement based on luminance-level modulation and gradient modulation," *Biomedical Signal Processing and Control*, vol. 48, pp. 189–196, 2019.

[22] A. W. Setiawan, T. R. Mengko, O. S. Santoso and A. B. Suksmono, "Color retinal image enhancement using CLAHE," in *Int. Conf. on ICT for Smart Society*, IEEE, pp. 1–3, 2013.

[23] P. K. Chaudhary and R. B. Pachori, "Automatic diagnosis of glaucoma using two-dimensional Fourier-bessel series expansion based empirical wavelet transform," *Biomedical Signal Processing and Control*, vol. 64, pp. 102237, 2021.

[24] D. Parashar and D. K. Agrawal, "Automatic classification of glaucoma stages using two-dimensional tensor empirical wavelet transform," *IEEE Signal Processing Letters*, vol. 28, pp. 66–70, 2020.

[25] D. Parashar and D. K. Agrawal, "Automated classification of glaucoma stages using flexible analytic wavelet transform from retinal fundus images," *IEEE Sensors Journal*, vol. 20, no. 21, pp. 12885–12894, 2020.

[26] L. Abdel-Hamid, "Glaucoma detection from retinal images using statistical and textural wavelet features," *Journal of Digital Imaging*, vol. 33, no. 1, pp. 151–158, 2020.

[27] C. S. F. Escamez, E. M. Giral, S. P. Martinez and N. T. Fernandez, "High interpretable machine learning classifier for early glaucoma diagnosis," *International Journal of Ophthalmology*, vol. 14, no. 3, pp. 393, 2021.

[28] F. Ajesh, R. Ravi and G. Rajakumar, "Early diagnosis of glaucoma using multi-feature analysis and DBN based classification," *Journal of Ambient Intelligence and Humanized Computing*, vol. 12, no. 3, pp. 4027–4036, 2021.

[29] D. Parashar and D. Agrawal, "Improved classification of glaucoma in retinal fundus images using 2D-DWT," in *2021 Int. Conf. on Advances in Electrical, Computing, Communication and Sustainable Technologies (ICAECT)*, IEEE, pp. 1–5, 2021.

[30] N. J. Shyla and W. S. Emmanuel, "Automated classification of glaucoma using DWT and HOG features with extreme learning machine," in *2021 Third Int. Conf. on Intelligent Communication Technologies and Virtual Mobile Networks (ICICV)*, IEEE, pp. 725–730, 2021.

[31] S. I. Khan, S. B. Choubey, A. Choubey, A. Bhatt, P. V. Naishadhkumar *et al.,* "Automated glaucoma detection from fundus images using wavelet-based denoising and machine learning," *Concurrent Engineering*, vol. 30, no. 1, pp. 103–115, 2022.

[32] L. K. Singh and M. Khanna, "A novel multimodality based dual fusion integrated approach for efficient and early prediction of glaucoma," *Biomedical Signal Processing and Control*, vol. 73, pp. 103468, 2022.